Nanoscale

Accepted Manuscript

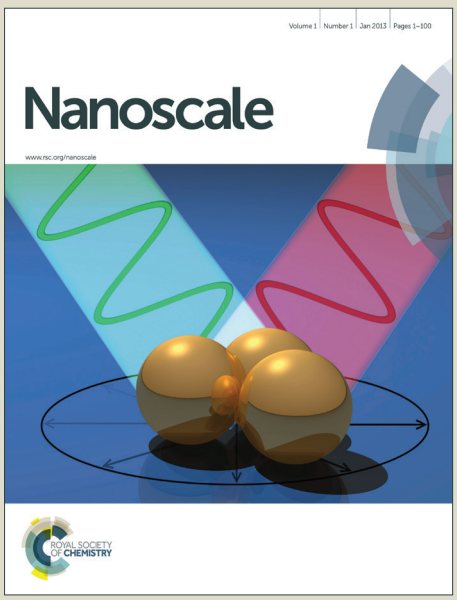

ROYAL SOCIETY OF CHEMISTRY

www.rsc.org/nanoscale

Cite this: DOI: 10.1039/c0xx00000x

www.rsc.org/ees

PAPER

Novel Li_2MnO_3 nanowire anode with internal Li-enrichment for lithium-ion battery†

Dandan Wang,‡ Yunlong Zhao,‡ Xu Xu, Kalele Mulonda Hercule, Mengyu Yan, Qinyou An, Xiaocong Tian, Jiaming Xu, Longbing Qu, Liqiang Mai,*

Received (in XXX, XXX) Xth XXXXXXXXX 20XX, Accepted Xth XXXXXXXXX 20XX
DOI: 10.1039/b000000x

Anode materials undergoing conversion reaction can achieve larger specific capacity than conventional carbon-based materials and can even achieve higher energy density when combined with the low and safe voltage. However, superabundant Li_2O generated in the interior of the structure upon lithium insertion causes the volume expansion and mechanical fracture from the inside out，which leads to poor cycling performance and limits their commercialization. To overcome aforementioned limitation, we introduced lithium atoms into the intracell of manganese oxide materials and successfully synthesized a novel Li-rich anode material (Li_2MnO_3). The reversible capacity reaches 1279 mAh g^{-1} after 500 cycles, much higher than that of pure MnO_2 or other commercial anodes. Additionally, the internal Li-enrichment optimization and the low-voltage lithium-ion battery anode Li_2MnO_3 nanowires are rarely reported. Further investigations by X-ray diffraction and photoelectron spectroscopy suggest that the strategy of internal Li-enrichment optimization as well as the novel anode Li_2MnO_3 is promising for lithium-ion batteries.

Introduction

The current appetite for rechargeable lithium-ion batteries (LIBs) with high power and energy density has led to extensive interest in nanotechnology approach to obtain high-performance, low-cost and environmentally-friendly electrode (cathode/anode) materials.[1-9] As anode materials for LIBs, transition metal oxides, such as Cr_2O_3,[10] Fe_2O_3,[11] Co_3O_4,[12-14] CuO,[15] and MnO_2[16] provide tremendous opportunities to realize this goal compared to conventional carbon-based materials. MnO_2 has been studied for a long time as cathode material for LIBs or electrode material for supercapacitors due to its natural abundance, non-toxicity and cost effectiveness.[17-21] As a typical transition metal oxide, MnO_2 can also serve as a potential anode material: by utilizing all its possible oxidation states through a conversion reaction, it possesses high theoretical capacity (four electron transfers occur per manganese ion). However, poor cycling performance constitute the main drawback which limits its application as anode material for LIBs. As shown in Figure 1a (left), MnO_2 is compact before charging-discharging. After lithium ions' insertion into the crystal structure and their conversion reaction with MnO_2, Mn and Li_2O nanoparticles "*in situ*" formed electrochemically. However, serious crystal distortion and volume expansion lead to lattice stress and self-aggregation during charge-discharge cycle (Figure 1a, right), resulting in the loss of electrical contact and ultimately electrode failure.[22-23]

Previous strategies to overcome these problems include: (1) Reducing the particle size from micro scale to nano scale to accommodate the large volume change and shorten the Li ion's diffusion length.[24] (2) Coating carbon-based materials or conducting polymers to enhance the electronic conductivity.[25-30] (3) Constructing hierarchical nanocomposites to take full advantages of synergistic effect of different components.[31-35] These techniques can partly prevent the large volume expansion and the resultant loss of electrical contact, but they all belong to the external modification and the crystal deformation as well as the volume change still exists. Moreover, sophisticated synthetic process cannot deter the reversible specific capacity from inevitable capacity fading.

In comparison, if we introduce lithium atoms into the intracell of these anode materials undergoing conversion reaction and obtain the Li_xMO_y structure (Figure 1b), the "*in situ*" electrochemically formed M metal (specifically Mn in our case) and Li_2O can be dispersed during the conversion process, and accommodate larger space to buffer the volume expansion. Furthermore, this Li-enrichment method removes the requirement that the cathode must contain lithium in its original states and opens up new avenues of pairing Li-free electrodes for the next generation high-energy LIBs.[36] Although similar strategies, such as pre-lithiation, have been applied in intercalation reaction in order to increase their ionic diffusion and/or electronic conductivity,[37-39] to the best of our knowledge, this strategy and its function are rarely reported for conversion reaction of anode materials.

In this work, we successfully synthesize a novel Li-rich anode material (Li_2MnO_3) for LIBs by inserting lithium atoms in manganese oxide. Completely different from rapid capacity fading of MnO_2, Li_2MnO_3 exhibits a very stable cycling performance and capacity over 1200 mAh g^{-1}, much higher than conventional carbon-based materials and other commercial

anodes. Studies of diffraction, modeling and photoelectron spectroscopy reveal that the pre-inserted Li in the manganese oxide lattice plays a key role for stabilization. Electrochemical performance and mechanism investigation further demonstrate that this novel and general strategy as well as the optimized anode Li_2MnO_3 is promising for LIBs.

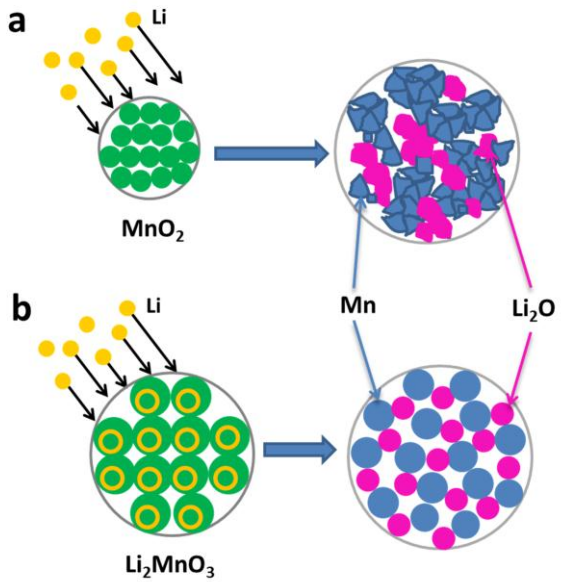

Figure 1 Schematic illustration of the behavior of (a) manganese oxide electrode that shows failure of the electrode because of crystal and volume change. (b) Our internal Li-enrichment anode Li_2MnO_3 electrode that shows a well-maintain of electrical contact between the metallic manganese nanoparticles and Li_2O.

Experimental section

Materials

For typical synthesis, $C_4H_6MnO_4•4H_2O$, $LiOH•H_2O$, H_2O_2, sodium dodecyl benzene sulfonate (SDBS), polyvinylpyrrolidone (PVP K30) were analytical reagent grade, purchased from Sinopharm Chemical Reagent Co. Ltd., Shanghai, China. All chemicals were used as received without further treatment.

Methods

Sample Synthesis: The Li_2MnO_3 nanowires were prepared in two steps. First, the MnOOH nanowires were synthesized by a hydrothermal method. SDBS (0.769 g) and PVP K30 (0.4446 g) were dissolved in deionized water of 50 ml. Meanwhile, $C_4H_6MnO_4•4H_2O$ (1.725 g) and LiOH (0.555 g) were dissolved in deionized water of 15 ml, respectively. And H_2O_2 (0.6 ml) was added. The as obtained solutions were mixed sequentially under continuous stirring. And then the final solution was transferred into a 100 ml Teflon-lined stainless steel autoclave and kept in an electric oven at 140 ^oC for 12 h. Later the autoclave was left to cool naturally to room temperature. The obtained precursors MnOOH nanowires were centrifuged, washed several times with distilled water and ethanol, and then dried at 110 ^oC in a vacuum oven. Second, the obtained MnOOH nanowires and $LiOH·H_2O$ were mixed (Mn : Li = 1:2) in alcohol and stirred for 12 h to obtain a homogeneous mixture. Finally, the mixture was heated at 70 ^oC to allow the alcohol evaporation and then annealed at 650 ^oC for 15 h in air to obtain red powder. For comparison, the MnO_2 nanowires were synthesized by annealing the precursor at 300 ^oC for 2 h (Figure S2 in the Supporting Information).

Characterizations

X-ray diffraction (XRD) measurements were performed to investigate the crystallographic information using a D8 Advance X-ray diffractometer with non-monochromated Cu-Ka X-Ray source. Field-emission scanning electron microscopy (FESEM) images were collected with a JEOL JSM-7100F at an acceleration voltage of 10 kV. Transmission electron microscopy (TEM) and high-resolution transmission electron microscopy (HRTEM) images were recorded by using a JEM-2100F STEM. X-ray photoelectron spectroscopy (XPS) was measured by VG Multilab 2000.

Electrochemical Measurements

The electrochemical properties were carried out by assembling 2016 coin cells in a glove box filled with pure argon gas, which use lithium pellets as the counter electrode and reference electrode, a 1 M solution of $LiPF_6$ in ethylene carbon (EC)/ dimethyl carbonate (DMC) (1:1 w/w) as electrolyte, anode electrodes were obtained with 70% Li_2MnO_3 nanowires active material, 20% acetylene black and 10% poly (tetrafluoroethylene) (PTFE). Galvanostatic charge/discharge cycling was studied in a potential range of 3.0–0 V *vs*. Li/Li^+ with a multichannel battery testing system (LAND CT2001A). Cycling Voltammetry (CV) and AC-impedance tests were performed with an electrochemical workstation (CHI 760D and Autolab PGSTAT 302N).

Results and Discussion

To determine the phase structures of the as-obtained products, XRD measurements were conducted. Figure 2a shows XRD patterns of the synthesized nanowires indexed as Li_2MnO_3 monoclinic structure (JCPDS No.00-027-1252, a = 4.928 Å, b = 8533 Å, c = 9.604 Å and β = 99.5 °) with a space group of C2/m, this structure is the same as that of R3m layered rock salt. TEM investigation has been carried out. As shown in Figure 2b, the as-prepared product exhibits nanowires morphology. HRTEM investigation reveals that these nanowires are well crystalline, and the lattice fringe spacings of 2.42 and 2.13 Å correspond to the inter plane distance of (-131) and (040) of the monoclinic structure of Li_2MnO_3, respectively.

FESEM images provide insight into the morphology of the products. Figure 2c shows a FESEM image of the Li_2MnO_3 nanowires, which have diameters of 20-80 nm and smooth surfaces. Figure 2d shows the FESEM image of MnO_2 nanowires as control experiment. They all keep the nanowire structure and

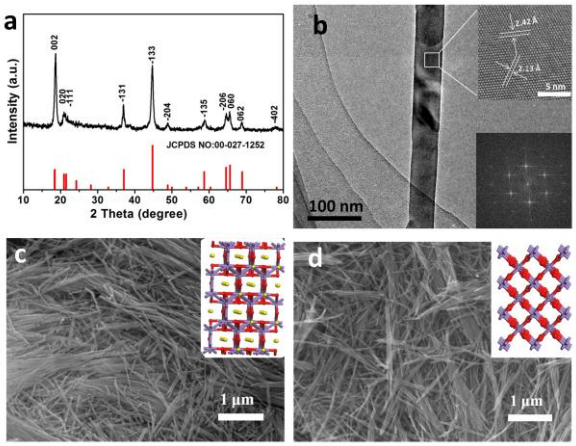

Figure 2 (a) XRD patterns of the Li_2MnO_3 nanowires. (b) TEM image of the Li_2MnO_3 nanowires. Inset is the HRTEM images of the Li_2MnO_3 nanowires. (c) SEM image of the Li_2MnO_3; Inset in c is the crystal structures of the Li_2MnO_3. (d) SEM image of the MnO_2. Inset in d is the crystal structures of the MnO_2. (The red ball represents O atoms, the purple one represents Mn atoms and the yellow represents Li atoms.)

are conformity with the nanowires morphology of the precursor MnOOH, which demonstrates that the process is a morphology conserved transformation (Figure S1b in the Supporting Information). The crystal structure of Li_2MnO_3 nanowires in the insets of the figure 2c indicates that the structure of Li_2MnO_3 is derived from the rhombohedral α-$NaFeO_2$ structure, with Li and Mn occupying the Na and Fe sites respectively. Unusually, one-third of the positions in the Mn-plane are replaced by Li to form an ordered $LiMn_2$ slab. The chemical formula of Li_2MnO_3 can be written as $\{(Li_{1/2})_{2c}(Li_1)_{4h}\}_{interslab}\{(Li_{1/2})_{2b}(Mn_1)_{4g}\}_{slab}(O_1)_{4i}(O_2)_{8j}$, in which the subscripts 2c, 4h, 2b, 4g, 4i, and 8j are the lattice sites occupied by the atoms in the round brackets. The sites within the Li layers are 2c and 4h, while the 2b site corresponds to the Li located in the $LiMn_2$ layer.[40] The volume of cell which occupied by 8 Mn atoms is 398.32×10^6 pm^3. While the crystal structure of MnO_2 nanowires in the inset of the Figure 2d can be indexed to a tetragonal phase which is composed of single chains of the octahedral structure.[41] The total volume of 4 cells is 222.56×10^6 pm^3, since the volume of cell which occupied by 2 Mn atoms is 55.64×10^6 pm^3. Through the actual calculation, the volume of internal Li-enrichment Li_2MnO_3 is 79.0% larger than that of MnO_2 with the same number of Mn atoms.

To explore the influence of Li-enrichment optimization on electrochemical performance, we fabricated coin cell and gained the CV performance, cycling and rate behavior of Li_2MnO_3 and MnO_2. CV results for Li_2MnO_3 nanowires are shown in Figure 3a, upper curve. The CV is measured at a sweep rate of 0.1 mV s^{-1} in the potential range from 0 V to 3.0 V *vs.* Li/Li^+ at room temperature. It is observed that upon the first scan, two cathodic peaks appear at 0.75 V and 0.08 V, respectively, corresponding to the reduction of lithium manganese oxide to metallic manganese (Mn^{4+} to Mn^0) and bivalent manganese ion (Mn^{4+} to Mn^{2+}) embedded in an amorphous matrix of Li_2O as well as the formation of Li_2O and a solid electrolyte interphase (SEI) layer.[42] First-discharge reaction involves destruction of the crystal structure (amorphization of lattice) followed by the formation of metallic nanoparticles embedded into the Li_2O matrix. One anodic peak located at 1.35 V can be seen, which indicates that the reoxidation of manganese proceeds in one step. The CV profiles of Li_2MnO_3 in the first three cycles are quite similar to those of the MnO_2 nanowires with some differences. The CV curve of Li_2MnO_3 in the third scan closely resembles to that of the second scan, which demonstrates that the lithiation and delithiation processes are highly reversible from the second cycle. Nevertheless, the CV curve of MnO_2 in the third scan still exhibits a reduced area.

Figure 3b-c are the primary cycling performance comparison of the two samples (MnO_2 nanowires and Li_2MnO_3 nanowires) at the current densities of 100 and 500 mA g^{-1}, respectively. The two samples have very similar electrochemical performance such as voltage platform but the Li_2MnO_3 nanowires show better cycling performance. The capacity of Li_2MnO_3 nanowires drop in the first few cycles, then increase over cycling , and finally get stabilized up to 10 cycles for the cell cycling at 100 mA g^{-1}. At current density of 100 mA g^{-1}, the second cycle discharge capacities of Li_2MnO_3 and MnO_2 nanowires are 1312 and 886 mAh g^{-1}, respectively. It is obvious that a significant loss of capacities happen at the first few cycles which may be attributed to decomposition of electrolyte and irreversible phase transition.[42] However, after 50 cycles, the discharge capacity of Li_2MnO_3 nanowires still remains 1184 mAh g^{-1}, while that of MnO_2 nanowires is only 637 mAh g^{-1}. Interestingly, the capacity gradually increases with the increasing cycle number. At the current density of 500 mA g^{-1}, even after 500 cycles, the discharge capacity of Li_2MnO_3 nanowires reaches 1279 mAh g^{-1}.

Furthermore, the rate capability of Li_2MnO_3 is tested at various current densities in the same potential window. The battery is charged and discharged at different rates ranging from 100 to 2000 mA g^{-1} (Figure 3d). The Li_2MnO_3 nanowires anode deliver the discharge capacities of 1311, 964, 745, 601, 440 and 251 mAh g^{-1}at current densities of 100, 200, 300, 500, 1000 and 2000 mA g^{-1}, respectively. Remarkably, even after this high-rate measurement, back at the current density of 100 mA g^{-1}, the capacity can reach 1422 mAh g^{-1}. This performance indicates the high reversibility of Li_2MnO_3 nanowires. The rate performance of Li_2MnO_3 nanowires is much better than the commercialized carbon-based materials[43] (~375 mAh g^{-1}) and $Li_4Ti_5O_{12}$[44] (~175 mAh g^{-1}).

It is noteworthy that the capacity of MnO_2 as anode material gradually decays during cycling, while the capacity of Li_2MnO_3 continuously increases. This significant difference indicates that there are substantial changes after optimization.

In order to understand the reaction mechanism of Li_2MnO_3, XPS tests were carried out to examine the change in the oxidation state of manganese before and after lithiaton (Figure 4a). The position and line shape (sharp Mn $2p_{3/2}$ peak at 641.9 eV and Mn $2p_{1/2}$ peak at 653.6 eV) of XPS spectra in Figure 4aI once again indicate the presence of the main quadrivalent manganese (Mn^{4+}). XPS spectra of Li_2MnO_3 nanowires after lithiaton (Figure 4a II) shows broader peaks of Mn 2p binding energy compared to the pristine electrode, indicating the presence of metallic manganese from the reduction of manganese oxide during lithiation process. The XPS spectra of the Li 1s peak centered at

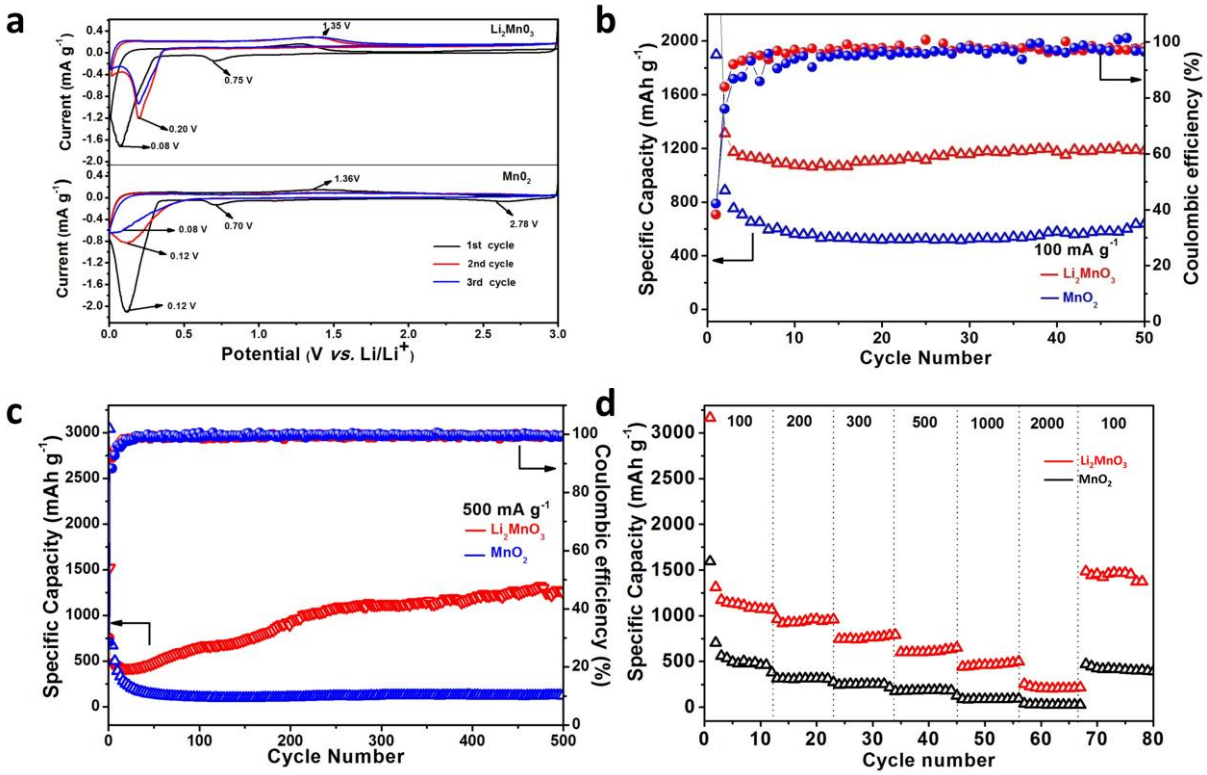

Figure 3 (a) Cyclic voltammetry curves at a sweep rate of 0.1 mV s^{-1} in the potential range from 3.0 to 0.0 V *vs.* Li/Li^+. (b-c) The cycling performances at the current density of 100 and 500 mA g^{-1}, respectively. (d) The rate performance of Li_2MnO_3 and MnO_2 nanowires.

55.3 eV confirms the formation of Li_2O (inset Figure 4aII). [16] The formation of Li_2O and metallic manganese during the initial lithiation process is thus confirmed, which indicate the electrochemical reaction taking place in Li_2MnO_3 is based on conversion reaction.

To follow the reaction process of Li_2MnO_3, we collected the XRD patterns at three states in the first discharge process (Figure 4b). The XRD patterns tested at initial point of 3.0 V (Figure 4b I) and at 0.3 V (Figure 4b II) show that both phases are identical to the Li_2MnO_3, indicating no phase transition before 0.3 V. As reported, the plateau at 0.75 V is in accordance with the process associated with reduction of the electrolyte. [45] The sloping region of the curve from 0.75 V to 0.3 V has previously been attributed to further SEI layer formation/electrolyte reduction on the surface of the composite electrode materials.[45] The XRD measured at the end of the discharge curve (Figure 4b III) indicates the presence of dominant phase of $Mn(OH)_2$ (associated with small amount of Li_2MnO_3). Considering the XPS data, metallic manganese also exist in the final product (because of the small size of metallic manganese, there is no diffraction peaks detected in XRD pattern[46]). Therefore we propose the following reaction:

$$Li_2MnO_3 + 2Li^+ + H^+ + 3e^- \rightarrow x\ Mn + (1\text{-}x)\ Mn(OH)_2 + 2Li_2O \quad (0 < x < 1) \quad (1)$$

After the insertion of 2Li, the gradual decrease in the discharge voltage is associated with the decrease of the LiOH (Figure 4aIII). Thus, a major reaction that contributes to the additional capacity in the Li/ Li_2MnO_3 system involves the conversion reaction of

$$LiOH + 2Li^+ + 2e^+ = Li_2O + LiH \quad (2)$$

which is at least partially reversible. Our results about contribution from H^+ and formation of LiH agree well with Clare P. Grey's results. [47]

To reveal the chemical changes during cycling of Li_2MnO_3 and further understand the enhanced cycling stability and the reason of continuous capacity increase, we compare the Mn 2p XPS spectra of Li_2MnO_3 at different cycle under 500 mA g^{-1}. After first discharge, there exist Mn^0, Mn^{2+} and Mn^{4+}, simultaneously (Figure 4a IV, A). Nevertheless, after first charge, Mn^0 disappears corresponding to the oxidation of manganese. The amount of Mn^0 is much less than that of Mn^{2+}, which is approximately equal to that of Mn^{4+}. (Figure 4a IV, B). After 200 discharge/charge, the XPS results show that the valence of manganese shift toward to the high state and the amount of Mn^0 is much less than that of Mn^{2+}, which is less than that of Mn^{4+}, indicating the amount of Mn $(OH)_2$ decreases and that of Li_2MnO_3 (or MnO_2) increases after long cycling (Figure 4a IV, C). The differences in the Mn valence during the electrochemical process can explain the capacity's increase during cycles. Different from the MnO_2 electrode in which the metallic manganese formed directly,[16] a mass of manganese hydroxide formed as buffer as well as the metallic manganese when it came to the Li_2MnO_3 electrode. From the above analysis, it is demonstrated that the Li-enrichment can act as electrochemical buffer on charging depth.

On the other hand, through the crystallographic analysis we also notice the crystal changes after Li-enrichment: the volume of internal Li-enrichment Li_2MnO_3 is 79.0% larger than that of MnO_2 with the same number of Mn atoms. These effects can alleviate the mechanical stress induced by the volume change and

the aggregation of the Mn nanoparticles during cycling. It is assumed that the pre-inserted Li in the manganese oxide lattice plays a key role in the dispersion of Mn nanoparticles embedded in the Li_2O matrix, which are expected to retain their high internal electrical contact after conversion during cycling. Thus, it is shown that Li-enrichment in metal oxide anode material can also exhibit physical buffer on volume expansion.

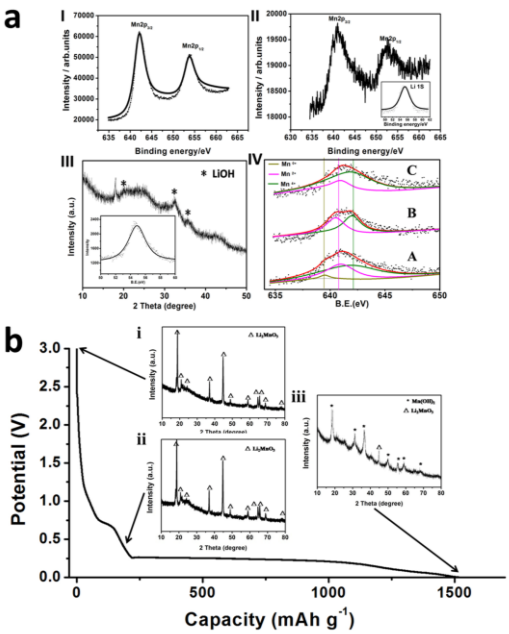

Figure 4 (a) XPS spectra of Li_2MnO_3 nanowires (I) before first lithium discharge process (II) after first lithium discharge process. Formation of manganese metal and Li_2O during the discharge process has been confirmed using XPS. (III) XRD and XPS patterns of LiOH. (IV) Mn 2p XPS spectra of (A) first lithium discharge (B) first lithium charge. (C) 200th lithium charge. (b) XRD patterns collected at various states of discharge for Li_2MnO_3 nanowires.

Conclusions

In summary, in order to fundamentally solve the problem of capacity fading in the conversion reaction material, that is, superabundant Li_2O generated in the interior of the structure upon lithium insertion causes the volume expansion and mechanical fracture from the inside out, we have brought up a strategy of internal Li-enrichment optimization and successfully synthesized novel Li_2MnO_3 nanowire anode material for LIBs. Electrochemical measurements suggest that anode material of Li_2MnO_3 nanowires undergoing conversion reaction exhibit an excellent performance in terms of reversible specific capacity, cycling stability and rate performance. The reversible capacity can reach 1279 mAh g^{-1} at the current density of 500 mA g^{-1} after 500 cycles, much higher than those of pure MnO_2 nanowires and other commercial anode materials. The studies of diffraction, modeling and photoelectron spectroscopy reveal that Li-enrichment in metal oxide anode material plays a key role for stabilization and acts as both electrochemical buffer on charge-discharge and physical buffer on volume expansion. Besides, this Li-enrichment method may remove the requirement that the cathode must contain lithium in its original states and opens up new avenues of pairing Li-free electrodes for the next generation high-energy LIBs. Thus, this new material as well as the optimization strategy will find great application in the energy storage field.

Acknowledgements

This work was supported by the National Basic Research Program of China (2013CB934103, 2012CB933003), the National Natural Science Foundation of China (51272197 and 51072153), the Program for New Century Excellent Talents in University (NCET-10-0661), the International Science & Technology Cooperation Program of China (2013DFA50840).

Notes and references

State Key Laboratory of Advanced Technology for Materials Synthesis and Processing, WUT-Harvard Joint Nano Key Laboratory, Wuhan University of Technology, Wuhan, 430070, P. R. China. Fax: +86-27-87644867; Tel: +86-27-87467595; E-mail: mlq518@whut.edu.cn

‡ These authors contributed equally to this work.

1 J. M. Tarascon, M. Armand, *Nature*, 2001, 414, 359-367.
2 B. Kang, G. Ceder, *Nature*, 2009, 458, 190-193.
3 H. G. Jung, M. W. Jang, J. Hassoun, Y. K. Sun, B. Scrosati, *Nat. Commun.*, 2011, 2, 516.
4 L. Ji, Z. Lin, M. Alcoutlabi and X. Zhang, *Energy Environ. Sci.*, 2011, 4, 2682-2699.
5 A. S. Aricò, P. Bruce, B. Scrosati, J. M. Tarascon and W. Van Schalkwijk, *Nat. Mater.*, 2005, 4, 366-377.
6 P. G. Bruce, B. Scrosati and J. M. Tarascon, *Angew. Chem., Int. Ed.*, 2008, 47, 2930-2946.
7 V. Etacheri, R. Marom, R. Elazari, G. Salitra and D. Aurbach, *Energy Environ. Sci.*, 2011, 4, 3243-3262.
8 B. Scrosati, J. Hassoun and Y. K. Sun, *Energy Environ. Sci.*, 2011, 4, 3287-3295.
9 F. Cheng, J. Liang, Z. Tao and J. Chen, *Adv. Mater.*, 2011, 23, 1695-1715.
10 L. Dupont, S. Laruelle, S. Grugeon, C. Dickinson, W. Zhou, J. M. Tarascon, *J. Power Sources* 2008, 175, 502-509.
11 M. Reddy, T. Yu, C. H. Sow, Z. X. Shen, C. T. Lim, G. Subba Rao, B. Chowdari, *Adv. Funct. Mater.*, 2007, 17, 2792-2799.
12 K. T. Nam, D. W. Kim, P. J. Yoo, C. Y. Chiang, N. Meethong, P. T. Hammond, Y. M. Chiang, A. M. Belcher, *Science* 2006, 312, 885-888.
13 Y. Cui, Z. Wen and Y. Liu, *Energy Environ. Sci.*, 2011, 4, 4727-4734.
14 F. Meng, Z. Fang, Z. Li, W. Xu, M. Wang, Y. Liu, J. Zhang, W. Wang, D. Zhao and X. Guo, *J. Mater. Chem. A*, 2013, 1, 7235-7241.
15 Y. Yu, Y. Shi, C. H. Chen, *Nanotechnology* 2007, 18, 055706.
16 A. L. M. Reddy, M. M. Shaijumon, S. R. Gowda, P. M. Ajayan, *Nano Lett.*, 2009, 9, 1002-1006.cc
17 F. Jiao, P. G. Bruce, *Adv. Mater.*, 2007, 19, 657-660.
18 J. Chang, M. Jin, F. Yao, T. H. Kim, V. T. Le, H. Yue, F. Gunes, B. Li, A. Ghosh, S. Xie, *Adv. Funct. Mater.*, 2013, 23, 5074-5083.
19 L. Peng, X. Peng, B. Liu, C. Wu, Y. Xie and G. Yu, *Nano Lett.*, 2013.
20 Q. Wang, J. Xu, X. Wang, B. Liu, X. Hou, G. Yu, P. Wang, D. Chen and G. Shen, *ChemElectroChem*, 2013.
21 L. Mai, H. Li, Y. Zhao, L. Xu, X. Xu, Y. Luo, Z. Zhang, W. Ke, C. Niu and Q. Zhang, *Scientific Reports*, 2013, 3.
22 J. Cabana, L. Monconduit, D. Larcher, M. R. Palacín, *Adv. Mater.*, 2010, 22, E170-E192.
23 M. Reddy, G. Subba Rao, B. Chowdari, *Chem. Rev.*, 2013.
24 S. Lee, Y. Cho, H. K. Song, K. T. Lee, J. Cho, *Angew. Chem., Int. Ed.*, 2012, 51, 8748-8752.
25 J. Guo, Q. Liu, C. Wang, M. R. Zachariah, *Adv. Funct. Mater.*, 2012, 22, 803-811.
26 B. Sun, Z. Chen, H. S. Kim, H. Ahn, G. Wang, *J. Power Sources*, 2011, 196, 3346-3349.

27 J. Liu, Q. Pan, *Electrochemical and Solid-State Lett.*, 2010, 13, A139-A142.
28 H. Xia, M. Lai, L. Lu, *J. Mater. Chem.*, 2010, 20, 6896-6902.
29 Y. Shi, J. Z. Wang, S. L. Chou, D. Wexler, H. J. Li, K. Ozawa, H.-K. Liu and Y. P. Wu, *Nano Lett.*, 2013, 13, 4715-4720.
30 F. Zou, X. Hu, L. Qie, Y. Jiang, X. Xiong, Y. Qiao and Y. Huang, *Nanoscale*, 2014, 6, 924-930
31 X. Gu, L. Chen, Z. Ju, H. Xu, J. Yang, Y. Qian, *Adv. Funct. Mater.*, 2013.
32 Y. M. Lin, R. K. Nagarale, K. C. Klavetter, A. Heller, C. B. Mullins, *J. Mater. Chem.*, 2012, 22, 11134-11139.
33 W. Zhou, C. Cheng, J. Liu, Y. Y. Tay, J. Jiang, X. Jia, J. Zhang, H. Gong, H. H. Hng, T. Yu, *Adv. Funct. Mater.*, 2011, 21, 2439-2445.
34 J. Zhu, Z. Lu, M. O. Oo, H. H. Hng, J. Ma, H. Zhang, Q. Yan, *J. Mater. Chem.*, 2011, 21, 12770-12776.
35 L. Q. Mai, F. Yang, Y. L. Zhao, X. Xu, L. Xu and Y. Z. Luo, *Nat. Commun.*, 2011, 2, 381.
36 N. Liu, L. Hu, M. T. McDowell, A. Jackson, Y. Cui, *ACS Nano* 2011, 5, 6487-6493.
37 X. Xu, Y. Z. Luo, L. Q. Mai, Y. L. Zhao, Q. Y. An, L. Xu, F. Hu, L. Zhang, Q. J. Zhang, *NPG Asia Mater.*, 2012, 4, e20.
38 M. W. Forney, M. J. Ganter, J. W. Staub, R. D. Ridgley and B. J. Landi, *Nano Lett.*, 2013, 13, 4158-4163.
39 M. R. Lukatskaya, O. Mashtalir, C. E. Ren, Y. Dall'Agnese, P. Rozier, P. L. Taberna, M. Naguib, P. Simon, M. W. Barsoum and Y. Gogotsi, *Science*, 2013, 341, 1502-1505.
40 R. Wang, X. He, L. He, F. Wang, R. Xiao, L. Gu, H. Li, L. Chen, *Adv. Energy Mater.*, 2013.
41 X. Wang, Y. Li, *J. Am. Chem. Soc.*, 2002, 124, 2880-2881.
42 M. Kundu, C. C. A. Ng, D. Y. Petrovykh, L. Liu, *Chem. Commun.*, 2013, 49, 8459-8461.
43 W. M. Zhang, J. S. Hu, Y. G. Guo, S. F. Zheng, L. S. Zhong, W. G. Song and L. J. Wan, *Adv. Mater.*, 2008, 20, 1160-1165.
44 C. Kim, N. S. Norberg, C. T. Alexander, R. Kostecki and J. Cabana, *Adv. Funct. Mater.*, 2012.
45 A. R. Armstrong, C. Lyness, P. M. Panchmatia, M. S. Islam, P. G. Bruce, *Nat. Mater.*, 2011, 10, 223-229.
46 P. Poizot, S. Laruelle, S. Grugeon, L. Dupont, J. Tarascon, *Nature* 2000, 407, 496-499.
47 Y. Y. Hu, Z. Liu, K. W. Nam, O. J. Borkiewicz, J. Cheng, X. Hua, M. T. Dunstan, X. Yu, K. M. Wiaderek, L.-S. Du, *Nat. Mater.*, 2013.

